Earth and Planetary Science Letters 353-354 (2012) 121–133 (reprint)

Contents lists available at SciVerse ScienceDirect

Earth and Planetary Science Letters

journal homepage: www.elsevier.com/locate/epsl

Anomalously steep dips of earthquakes in the 2011 Tohoku-Oki source region and possible explanations

Zhongwen Zhan [a,*], Don Helmberger [a], Mark Simons [a], Hiroo Kanamori [a], Wenbo Wu [b], Nadaya Cubas [c], Zacharie Duputel [a], Risheng Chu [a], Victor C. Tsai [a], Jean-Philippe Avouac [a], Kenneth W. Hudnut [d], Sidao Ni [e], Eric Hetland [f], Francisco H Ortega Culaciati [a]

[a] Seismological Laboratory, California Institute of Technology, 1200 E. California Blvd., Pasadena, CA 91125, USA
[b] School of Earth and Space Sciences, University of Science and Technology of China, Hefei, Anhui 230026, China
[c] Tectonic Observatory, California Institute of Technology, 1200 E. California Blvd., Pasadena, CA 91125, USA
[d] U. S. Geological Survey, 525, S. Wilson Ave, Pasadena, CA 91106, USA
[e] State Key Laboratory of Geodesy and Earth's Dynamics, Institute of Geodesy and Geophysics, CAS, Wuhan 430077, China
[f] Department of Earth and Environmental Sciences, University of Michigan, 2534 C. C. Little Building, 1100 North University Avenue, Ann Arbor, MI 48109, USA

ARTICLE INFO

Article history:
Received 19 May 2012
Received in revised form
26 July 2012
Accepted 27 July 2012
Editor: P. Shearer

Keywords:
subduction zone
the 2011 Tohoku-Oki earthquake
focal mechanism
fault geometry
seamount
fault zone structure

ABSTRACT

The 2011 M_w 9.1 Tohoku-Oki earthquake had unusually large slip (over 50 m) concentrated in a relatively small region, with local stress drop inferred to be 5–10 times larger than that found for typical megathrust earthquakes. Here we conduct a detailed analysis of foreshocks and aftershocks (M_w 5.5–7.5) sampling this megathrust zone for possible clues regarding such differences in seismic excitation. We find that events occurring in the region that experienced large slip during the M_w 9.1 event had steeper dip angles (by 5–10°) than the surrounding plate interface. This discrepancy cannot be explained by a single smooth plate interface. We provide three possible explanations. In Model I, the oceanic plate undergoes two sharp breaks in slope, which were not imaged well in previous seismic surveys. These break-points may have acted as strong seismic barriers in previous seismic ruptures, but may have failed in and contributed to the complex rupture pattern of the Tohoku-Oki earthquake. In Model II, the discrepancy of dip angles is caused by a rough plate interface, which in turn may be the underlying cause for the overall strong coupling and concentrated energy-release. In Model III, the earthquakes with steeper dip angles did not occur on the plate interface, but on nearby steeper subfaults. Since the differences in dip angle are only 5–10°, this last explanation would imply that the main fault has about the same strength as the nearby subfaults, rather than much weaker. A relatively uniform fault zone with both the main fault and the subfaults inside is consistent with Model III. Higher resolution source locations and improved models of the velocity structure of the megathrust fault zone are necessary to resolve these issues.

1. Introduction

The devastating 2011 M_w 9.1 Tohoku-Oki earthquake occurred on the megathrust where the Pacific Plate subducts below Japan at an average rate of about 8.0–8.5 cm/yr (DeMets et al., 2010). This earthquake was largely unexpected mainly due to the absence of large ($M > 8.3$) earthquakes in recorded history, despite evidence for a similar earthquake in 869 AD, the Jogan earthquake (Minoura et al., 2001; Usami, 1966). Geophysical observations of the Tohoku-Oki earthquake stem from global and regional broadband seismographic networks (e.g. Ammon et al., 2011; Ide et al., 2011; Lay et al., 2011), a near-field geodetic network (e.g. Ozawa et al., 2011; Simons et al., 2011), as well as ocean bottom measurements (e.g. Sato et al., 2011; Tsuji et al., 2011) and open ocean tsunami data (e.g. Simons et al., 2011). Earthquake slip models generated from various combinations of these datasets all display high co-seismic slip (25–50 m) in a relatively small region (~150 km by 100 km) (Fig. 1A). For comparison, models of the 2010 M_w 8.8 Maule, Chile, earthquake typically have twice the along-strike extent of slip and less than half the peak slip (Simons et al., 2011). The long recurrence time and concentrated region of large slip suggest the potential existence of barriers that support high stress accumulation before they rupture. Under this hypothesis, such barriers may pin the fault locally, limiting the amount of seismic slip occurring in neighboring areas that have lower thresholds for failure.

* Corresponding author. Tel.: +1 626 395 6971; fax: +1 626 564 0715.
E-mail addresses: zwzhan@gps.caltech.edu, zwzhan@gmail.com (Z. Zhan).

0012-821X/$ - see front matter © 2012 Elsevier B.V. All rights reserved.
http://dx.doi.org/10.1016/j.epsl.2012.07.038

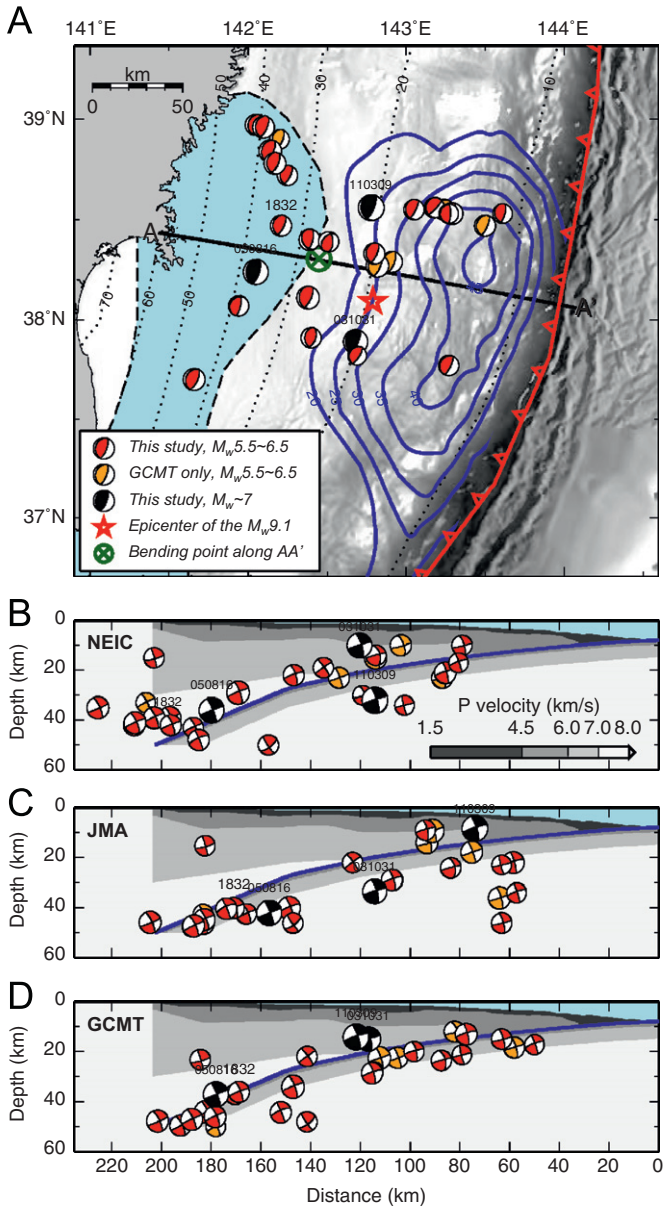

Fig. 1. Locations of events occurring along the megathrust. (A) Map view of our study area. Blue contours are the co-seismic slip model of the 2011 Tohoku-Oki earthquake from Wei et al. (2012). The light blue area shows the source area of high frequency radiation as imaged by back-projection method (Koper et al., 2011). AA' is a seismic reflection and refraction profile (Miura et al., 2005), whose result is shown in Fig. 1B. Colored beachballs (see legend) indicate all the $M_w > 5.5$ shallow-angle thrust earthquakes near the AA' profile (< 60 km), except the 2011 Tohoku-Oki earthquake. The red star indicates the epicenter location of the Tohoku-Oki earthquake determined by an Ocean-Bottom-Seismometer (OBS) network (Suzuki et al., 2012). (B) Greyscale background shows the 2D P wave velocity model along AA' profile, from Miura et al. (2005). The blue line is the reference plate interface at the top of the low-velocity oceanic crust. Colored beachballs (see the legend in (A)) show the NEIC locations of the earthquakes, projected to the AA' profile. (C, D) Similar to (B), but for JMA and GCMT, respectively. The red beachball labeled 1832 is the December 16, 2005, 18:32 M_w 6.0 earthquake, discussed later as an example event. Note the inconsistencies among earthquake locations, especially depths, from different catalogs. (For interpretation of the references to color in this figure caption, the reader is referred to the web version of this article.)

When the strongest barrier finally ruptures, the surrounding areas can catch up (Simons et al., 2011). Several candidates for barriers, including subducted seamounts and bending of the oceanic plate, have been proposed by Fukao et al. (2011). Zhao et al. (2011) suggest that the high stress drop may be controlled by structural heterogeneities in the megathrust zone.

Another important aspect of the Tohoku-Oki earthquake is the depth variation of seismic wave radiation. While co-seismic slip models show that large slip occurred updip of the hypocenter (e.g. Lay et al., 2011; Shao et al., 2011b; Simons et al., 2011; Wei et al., 2012), the majority of back-projection methods locate most coherent high-frequency (~1 Hz) radiation downdip of the hypocenter (e.g. Koper et al., 2011; Simons et al., 2011; light blue area in Fig. 1A). This spatial offset between large slip and high-frequency radiation is also reported for other megathrust earthquakes, such as the 2004 Sumatra-Andaman earthquake and the 2010 Chile earthquake (e.g. Lay et al., 2012). This depth variation in seismic radiation may suggest along-dip variations in mechanical or frictional properties (Lay et al., 2012; Simons et al., 2011), but the physical cause is still unclear.

To better understand the Tohoku-Oki earthquake's large stress drop and the offset between the areas of large slip and high-frequency radiation, we need more information about the megathrust's properties. Small to moderate interplate earthquakes have been widely used to extract mechanical properties on and around the plate interface. For example, Hasegawa et al. (2007) used repeating earthquakes to infer the coupling rate on the megathrust. Zhao et al. (2011) inverted earthquake travel times for a P wave velocity model around the plate interface. By studying seismic source spectra for M_w 6.0–7.6 earthquakes, Ye et al. (in press) showed depth dependent stress drops.

In this paper, we use the locations and focal mechanisms of all $M_w \geq 5.5$ earthquakes in the source area of the Tohoku-Oki earthquake to systematically study the geometry of the plate interface. We first discuss potential biases and uncertainties in earthquake locations and focal mechanisms from routine catalogs. Due to these issues, we explore high-resolution methods to re-estimate earthquake depths and focal mechanisms using available velocity models in the Tohoku-Oki region. We find that interplate earthquakes in this area occurred close to the plate interface imaged in previous seismic surveys, but there is a clear depth-dependent dip angle discrepancy. Three possible explanations of the discrepancy and their pros/cons are discussed.

2. Routine catalogs and previous Studies

Earthquake locations and focal mechanisms of $M_w \geq 5.5$ earthquakes around the globe are reported by many routine catalogs. However, these routinely determined results have significant inconsistencies as displayed in Fig. 1. For the Tohoku-Oki source region, Fig. 1B–D compares the projected locations of M_w 5.5–7.5 shallow-angle thrust earthquakes on the AA' profile (Fig. 1A), based on the National Earthquake Information Center (NEIC), the Japan Meteorological Agency (JMA) and the Global Centroid Moment Tensor (GCMT) catalogs, respectively. The NEIC catalog's horizontal locations are systematically shifted to the west of the JMA and GCMT locations by about 20 km. JMA's and GCMT's horizontal locations are relatively consistent near the Japan coast, but less consistent towards the trench. Depths are even less well resolved for the three catalogs. The uncertainty in earthquake locations, especially depths, makes it hard to distinguish between interplate and intraplate earthquakes.

Earthquake focal mechanisms or moment tensor solutions also have similar difficulties. Most routine catalogs of earthquake focal mechanisms do not have (meaningful) error estimation. By comparing focal mechanisms from different catalogs (e.g. the GCMT catalog and the USGS CMT catalog) between 1977 and 2003, Kagan (2003) shows that for shallow $M \geq 6$ earthquakes, the average 3D rotation angle is about 20°. However, the uncertainties of different

focal mechanism parameters (strike, dip and rake) were not addressed. Depending on the wave types and inverse method, particular focal mechanism parameters could be well resolved. For example, if teleseismic P waves are used to constrain a shallow-angle thrust focal mechanism as displayed in Fig. 2, the steep fault plane (denoted as Plane2 in Fig. 2B, described by strike2 and dip2) is well sampled and resolved. The shallow-angle fault plane (Plane1) is related to Plane2 by rake2, which could have a larger uncertainty. Fig. 2C shows the scatter of focal mechanisms with perfectly constrained strike2 and dip2, but rake2 with a Gaussian error (std=5°). The corresponding distributions of strike2, dip2, rake2, strike1, dip1 and rake1 are shown in (D, E, F, G, H, I). Although strike1 and rake1 have large uncertainties, dip1 (especially its lower limit) is well constrained. It is this dip angle that we focus on here.

There is significant moment-dip-depth tradeoff in inversions of focal mechanisms for shallow earthquakes determined by long-period surface waves (e.g. Kanamori and Given, 1981; Tsai et al., 2011). This tradeoff is generally not explicitly addressed in routine catalogs. Due to these difficulties, the interpretation of focal mechanisms in terms of plate interface geometry is not straight-forward. For example, Hayes et al. (2009) observed a systematic difference between the dips of their inverted plate interface model and the dips of GCMT moment tensors, but could not fully resolve whether this difference was real or related to focal mechanism bias.

The source area of the Tohoku-Oki earthquake is ideal for high-resolution study because of the availability of detailed crustal surveys. Using reflection and refraction data from an active source seismic experiment with 36 ocean bottom seismographs (OBS), Miura et al. (2005) and Ito et al. (2005) presented seismic profiles along AA' shown in Fig. 1A. The 2D P wave velocity model from Miura et al. (2005) is shown as gray-scale background in Fig. 1B–D. The plate interface can be easily identified as the top of the low velocity oceanic crust (blue lines). In this plate interface model, there is a kink at about 150 km from the trench, at a depth of ~28 km (see Fig. 1A for a map view and B for side view), where the dip angle jumps from 13° to 23°. Although the ray coverage and resolution values indicate well-resolved model parameters, it should be noted that this velocity model and plate interface model are smoothed due to damping during inversion, and therefore only represent large-scale features. For example, Ito et al. (2005) presented a slightly different model using a similar dataset but a different inverse method. We use the Miura et al. (2005) plate interface model as our reference model, and differences that would result from using different models are described in Section 5. For our purposes, locations (especially depths) of events with respect to the plate boundary are important.

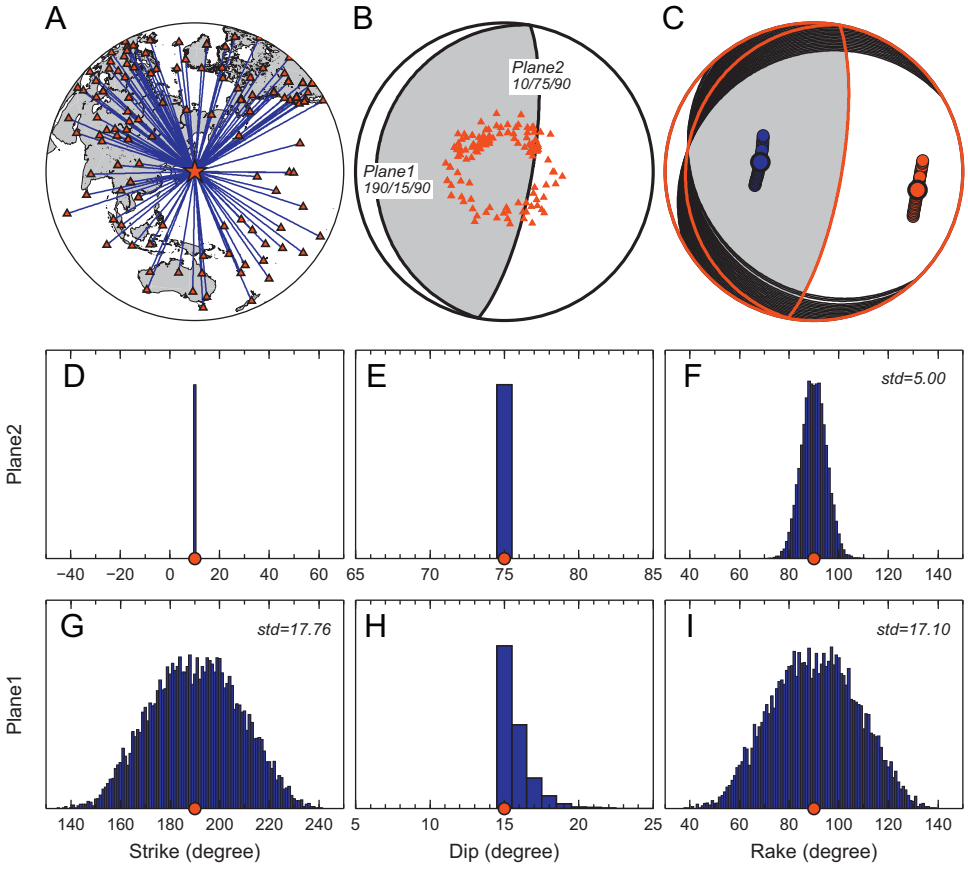

Fig. 2. Sensitivity analysis of focal mechanism parameters. (A) Map view of the Global Seismographic Network (GSN) and International Federation of Digital Seismograph Networks (FDSN) stations used in this study (red triangles). Note the good azimuthal coverage with respect to our study region (red star). (B) Sampling of teleseismic body waves (red triangles) on the lower hemisphere of a typical shallow-angle thrust focal mechanism in this region. Apparently Plane2 (described by strike2, dip2) is well sampled, while Plane1 (described by strike1, dip1) is not. Plane1 and Plane2 are related by the rake angles (rake1, rake2). (C) Scatter of focal mechanisms (black lines and small dots) when strike2 and dip2 are perfectly constrained but rake2 has a Gaussian error with std=5°. The focal mechanism shown with the red line is the same as in (B). Red dots and blue dots indicate the *P* axes and *T* axes, respectively. The corresponding distributions of strike2, dip2, rake2, strike1, dip1 and rake1 are shown in (D, E, F, G, H, I). Although strike1 and rake1 have large uncertainties, dip1 (especially its lower limit) is well constrained. (For interpretation of the references to color in this figure caption, the reader is referred to the web version of this article.)

As shown in Fig. 1, while the JMA and GCMT horizontal locations have no systematic differences, the NEIC horizontal locations are offset ~20 km toward the coast. Suzuki et al. (in press) show that the JMA catalog near the coast does not have a systematic bias with respect to the catalog determined by OBS data. Because the quality of the JMA catalog drops toward the trench and the GCMT catalog appears to be most compatible with the OBS catalog, we will use GCMT catalog's horizontal locations in what follows. We consider all the M_w 5.5–7.5 interplate earthquakes over the time period from 1994 to mid-2012 near this seismic profile, and compare them with the reference plate interface model.

3. Methods

To avoid potential effects of strong lateral variations of seismic structure, we confined our study area to lie within a 120 km band centered around the AA' profile (Fig. 1A). Since we are mainly interested in interplate earthquakes, we studied all the shallow-angle thrust events in this area from 1994 to the present (M_w 5.5–7.5 in the GCMT catalog). We used all available Global Seismographic Network (GSN) and International Federation of Digital Seismograph Networks (FDSN) seismograms to ensure a relatively uniform azimuthal coverage (Fig. 2A). We present our high-resolution waveform analysis in detail for an example event (2005/12/16, 18:32 M_w 6.0, see Fig. 1 for event information reported by the various organizations). We first invert for earthquake depths using broadband teleseismic P waves (Fig. 3); then we invert for focal mechanisms using longer period teleseismic P and SH body waves and explore the uncertainties of different parameters (Fig. 4).

3.1. Earthquake Depths

Earthquake depths are not well constrained in routine catalogs as shown in Fig. 1B–D because only long-period waves or travel-time information are used in most cases. Accurate depth determination requires fitting relatively broadband waveforms including direct and depth phases taking into account a local seismic velocity model in the source region. The local high-resolution 2D tomographic model (Fig. 1B) allows for broadband waveform modeling. For each earthquake, we only choose high signal-to-noise ratio (SNR) broadband (2–50 s period) vertical-component P wave packages (P+pP+sP) to estimate depth (Fig. 3A). Synthetic seismograms are calculated with a 1D source-side velocity model extracted from the 2D velocity model (Fig. 1B) based on the earthquake's projected location on AA' (e.g. Kikuchi and Kanamori, 1982). We grid-search earthquake depth, duration and focal mechanism to best fit the normalized waveform. Note that due to large variations in broadband P wave amplitudes, we do not invert for seismic moment. As a typical example, Fig. 3 shows the depth inversion and best waveform fits for the 2005/12/16, 18:32 M_w 6.0 earthquake, whose misfit curves have a well-defined minimum at 35 km, with little tradeoff with earthquake duration. This accurate estimation of earthquake depth will benefit our later focal mechanism inversion by largely removing the depth tradeoff.

Since the broadband P wave package includes the sP phase, and the 2D velocity model is only based on P waves, we generate an *S* velocity model by assuming a Vp/Vs ratio. Brocher (2005) compiled several different Vp/Vs measurements, and derived an empirical relation between Vp/Vs and Vp. The suggested average Vp/Vs is ~1.73. However, Suzuki et al. (in press) noticed that this forearc area may have a relatively high Vp/Vs ratio. Takahashi et al. (2002) determined both Vp and Vs velocity models along a high-resolution seismic profile in the forearc region of the Nankai Trough, and they also found higher Vp/Vs values. In this study, we use an average Vp/Vs ratio of ~1.87 from Takahashi et al. (2002). Tests show that different Vp/Vs ratios could cause systematic differences in earthquake depths (e.g. $\leq$3 km for Vp/Vs=1.73 or 1.87), but have little effect on earthquake focal mechanisms.

3.2. Earthquake focal mechanisms

We first determine the depth of each earthquake as described above and then we fix the depth and invert for focal mechanism. For M_w 5.5–6.5 earthquakes, 15–50 s period-band teleseismic P and SH wave packages are fitted by grid-searching moment, strike, dip and rake. The waveform fit is insensitive to earthquake duration due to the longer period band than typifies the duration of $M_w < 6.5$ earthquakes. We treat $M_w \sim 7$ earthquakes slightly differently, as discussed later. Fig. 4A shows example P and SH seismograms for the 2005/12/16, 18:32 M_w 6.0 earthquake, sorted by azimuth. Note the clear variation of both P and SH waveform and amplitudes with azimuths, which we use as a constraint on the focal mechanism. P waves are weighted twice as much as SH waves to compensate for the overall smaller amplitudes. Teleseismic SH waves are known to be noisier than P waves due to generally noisier horizontal components and contamination from sPL waves (Helmberger and Engen, 1974), so we have a higher quality control for SH waves. A group of six earthquakes close to

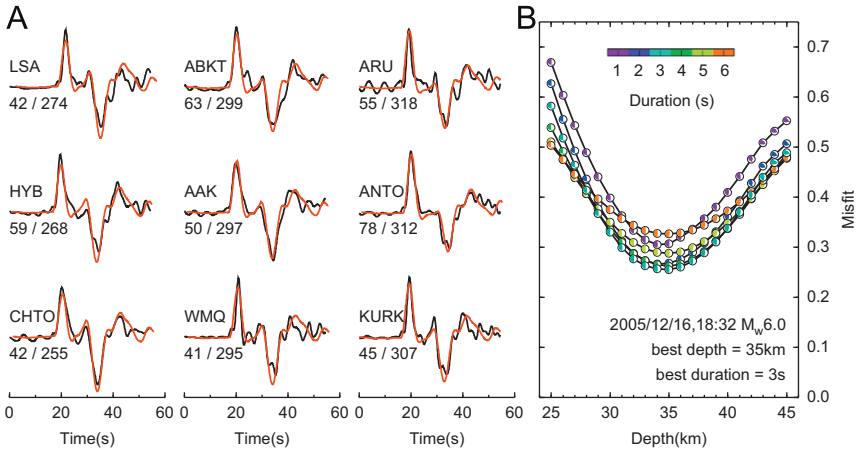

Fig. 3. Estimation of earthquake depths using broadband teleseismic P waves with depth phases. (A) Examples of waveform fit for the 2005/12/16 M_w 6.0 earthquake. Data and synthetics seismograms are shown in black and red, respectively. The two numbers below each station name are epicentral-distance and azimuth in degrees. (B) Waveform misfits as a function of grid-searched earthquake depth and duration. (For interpretation of the references to color in this figure caption, the reader is referred to the web version of this article.)

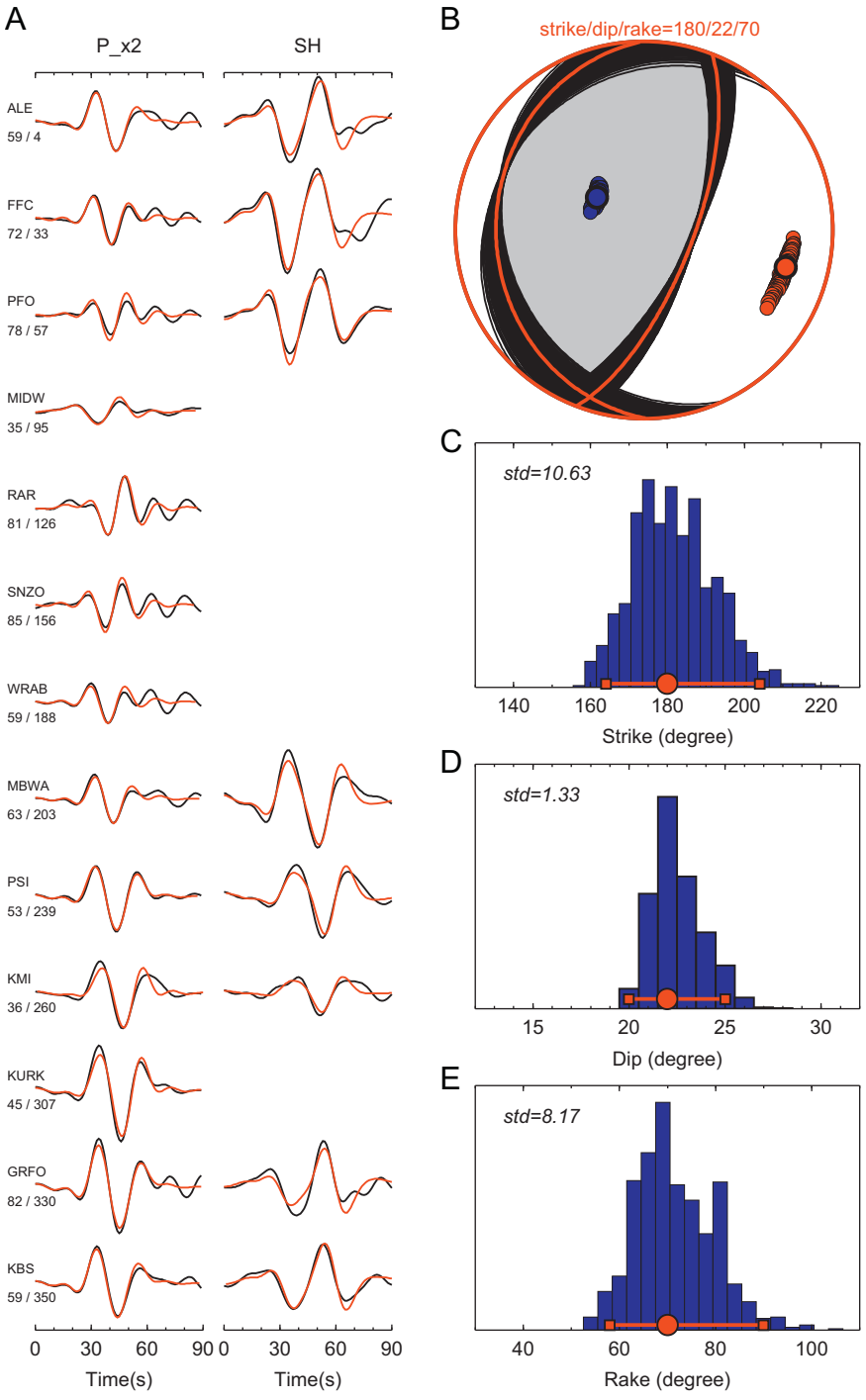

Fig. 4. Focal mechanism inversion using 15–50 s period-band teleseismic P and SH waves. (A) Examples of waveform fit for the 2005/12/16 M_w 6.0 earthquake. Data and synthetic seismograms are shown in black and red, respectively. The two numbers below each station name are epicentral-distance and azimuth in degrees. P waves are multiplied by a factor of 2 to balance the larger SH amplitudes. Due to the higher quality control for SH, we usually have more P wave records than SH waves. (B) Red beachball and big dots show the best fit solution. We perform bootstrapping analysis to estimate the confidence limits. Black beachballs and small dots show the bootstrapping results. Red and blue dots indicate the *P* axes and *T* axes, respectively. (C, D, E) display the histograms of strike, dip and rake of the bootstrapping results, respectively. As quantified by the standard deviation (std shown in the upper-left corners) dip is constrained much better than strike and rake. Red dots represent the optimal values. Red squares and red lines indicate the corresponding 95% confidence limits, estimated by removing 2.5% on both sides of the histograms. (For interpretation of the references to color in this figure caption, the reader is referred to the web version of this article.)

the coast are chosen to be benchmark events as they are relatively easy to study, even with only P waves. We require that the SH waveform fits have cross correlation coefficients higher than 90% for all the benchmark events. This requirement filtered out about half of the SH records. Fig. 4A, B displays the best waveform fits and optimal focal mechanism in red for the 2005/12/16, 18:32 M_w 6.0 earthquake.

As mentioned earlier, focal mechanism inversions for shallow earthquakes using long-period surface waves are subject to a significant moment-dip-depth tradeoff (e.g. Kanamori and Given, 1981; Tsai et al., 2011). Since we estimate earthquake depths independently using broadband P waveforms, we only have the moment-dip tradeoff problem to deal with. As there is no theoretical study about this tradeoff for the case when using

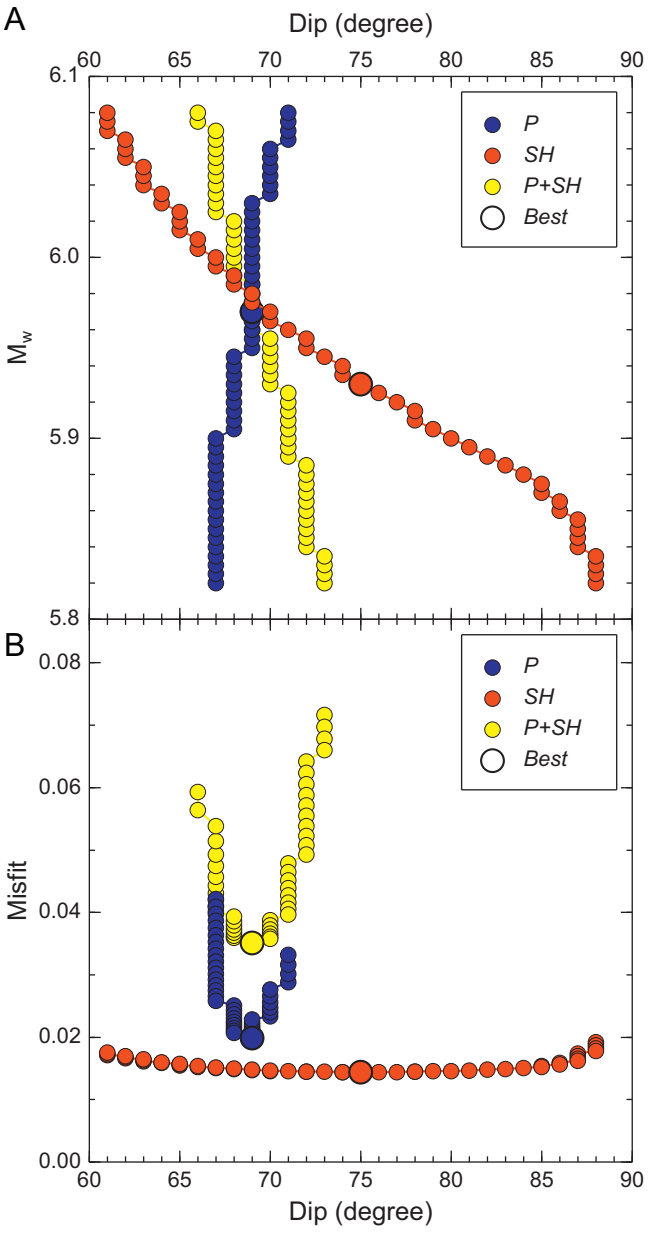

Fig. 5. Moment-dip tradeoff for teleseismic P and SH waves. (A) The M_w-Dip tradeoff curves for P only, SH only and P+SH in blue, red and yellow dots, respectively. The best solutions with least waveform misfit for each case are indicated by larger dots. (B) The corresponding waveform misfits as a function of dip angle. Colors and sizes of dots are the same as in (A). (For interpretation of the references to color in this figure caption, the reader is referred to the web version of this article.)

relatively broadband teleseismic body waves, we performed an empirical check for each earthquake. Fig. 5A shows the relations between M_w and dip angle for inversions using only P waves (blue dots), SH wave only (red dots) and P+SH waves (yellow dots). The SH-only case has a much stronger moment-dip tradeoff than P-only or P+SH. Also the moment-dip tradeoff for the SH-only case is very severe because the misfits do not change much along the tradeoff curve (flat red curve in Fig. 5B). However, the P-only case shows a much sharper misfit curve, which means the moment-dip tradeoff is much less significant for P waves. The reason for this is that depth phases pP and sP interfere with each other (opposite-sign) making the waveforms very sensitive to dip-angle. As expected, the P+SH case is dominated by P waves.

Due to the non-linear characteristics of waveform inversion, it is not trivial to assess the accuracy of the result. Here we apply the bootstrapping method to estimate 95% confidence intervals (e.g. Tichelaar and Ruff, 1989). In detail, we independently resample the N (~80) stations used in the inversion M times (where M is a large number, e.g. 10,000), each with N stations but with some station duplication and some stations not being sampled. We then analyze each sampled dataset in the same way as the original dataset to estimate the source parameters. The confidence intervals and other statistical quantities can be estimated from these M results. Note that our grid-searching methodology requires little additional computation time for the bootstrapping process, because we can store the waveform misfits for each station and focal mechanism in the first grid-search step. In this study, obtaining an accurate fault geometry from earthquake focal mechanism is critical, so we estimate the 95% confidence limits of strike, dip and rake by evaluating the point corresponding to 2.5% from each end of the distribution of the M results (Fig. 4C–E). The M bootstrapping focal mechanisms are also plotted in Fig. 4B in black to show the rotation angles. While strike and rake have large uncertainties (std~10°), the dip angle is well constrained (Fig. 4). This behavior is expected for inversions using teleseismic body waves, as shown by the sensitivity test in Fig. 2.

Because 1D velocity models extracted from a 2D tomography model are used in the inversions, we consider the potential bias caused by the dipping velocity structure on our estimates of the earthquake focal mechanisms, especially dip angles. The west-dipping subducting slab and east-dipping seafloor are the two major dipping structures. To assess the effect of dipping source-side structure on focal mechanism, we conduct a synthetic test. It is not trivial to calculate synthetic seismograms for $T \geq 15$ s teleseismic body waves and take into account the detailed

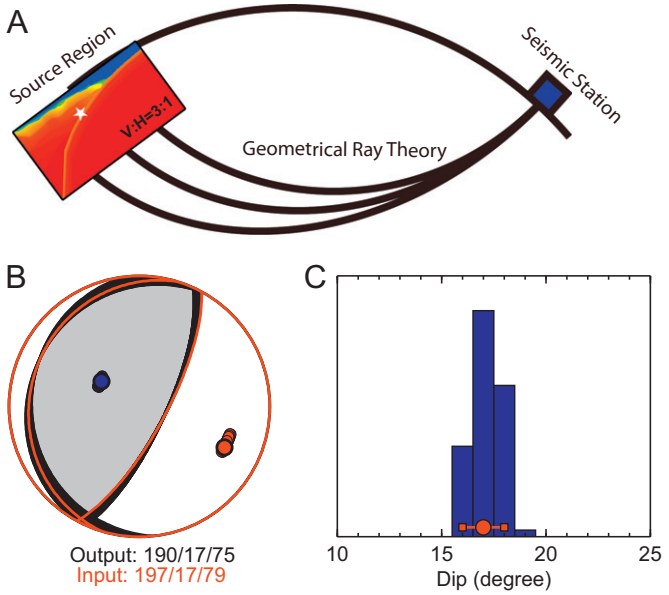

Fig. 6. Synthetic test of 3D source-side structure's effect on focal mechanism inversion with a hybrid method. (A) Sketch illustrating the hybrid method. In the source region, we use the SEM to fully take into account the 3D structure, including the water layer and slow sediment layers. White star shows the earthquake location. On the boundary of the source region, SEM is interfaced with geometrical ray theory to calculate the teleseismic body waves recorded at seismic stations. (B) The input focal mechanism is shown in red beachball and big dots. The inverted focal mechanisms with bootstrapping results are shown as a black beachballs and small dots. Red and blue dots are P axes and T axes, respectively. (C) Histogram of the inverted dip angles. Red dots are the optimal values. Red squares and red lines indicate the corresponding 95% confidence limits.

source-side structure with a dipping water layer and slow sediment layers. We designed a hybrid method which interfaces the Spectral Element Method (SEM, Komatitsch and Tromp, 1999) in the source area with geometrical ray theory elsewhere (Fig. 6A). More details about this hybrid numerical method will be presented in another paper (Wu et al., in preparation). In the synthetic test, we estimate the focal mechanism and 95% confidence intervals using the same procedures discussed above and result is shown in Fig. 6B. Ignoring 3D source-side structure causes some scatter in the focal mechanism, but no systematic bias is observed. For the best constrained parameter, the dip angle, the scatter is on the order of 1° (Fig. 6C), smaller than the uncertainties observed for real data (e.g. Fig. 4D).

3.3. $M\sim7$ earthquakes

There are three $M_w\sim7$ events in our catalog, shown as black beachballs in Fig. 1: 2003/10/31, 01:06, M_w 6.9; 2005/08/16, 02:46, M_w 7.3; 2011/03/09, 02:45, M_w 7.3. Due to the longer source durations and more complicated source time functions, the depth phases cannot be easily identified or fit to estimate the depths and we therefore use a slightly different approach to modeling these events. We adopt the latitude and longitude of the GCMT centroid and adjust the depths such that they occurred on the assumed reference plate interface. During the focal mechanism inversion, we use a longer period band (25–50 s) to ensure the validity of the point source approximation. The 95% confidence intervals are estimated applying the above bootstrapping method.

4. Results

We studied a total of 28 shallow-angle thrust events (details in Table S1), two of which are located more than 5 km away from the reference plate interface hence considered intraplate, five of which are too noisy for body-wave waveform modeling due to interference from events close in time so we just adopt their GCMT solutions (orange color in Fig. 1 and Fig. 7). Fig. 7 shows the results for the other 21 events, including the 3 $M_w\sim7$ events. Five of these events are aftershocks of the Tohoku-Oki earthquake, and they all occurred downdip of the large slip area. Using the GCMT horizontal locations and the re-estimated depths, these earthquakes are located along the reference plate interface, with significant improvement compared with the locations from routine catalogs shown in Fig. 1. Since these earthquakes all have shallow-angle thrust mechanisms, we assume that they are interplate earthquakes. This assumption is also supported by their source spectra.

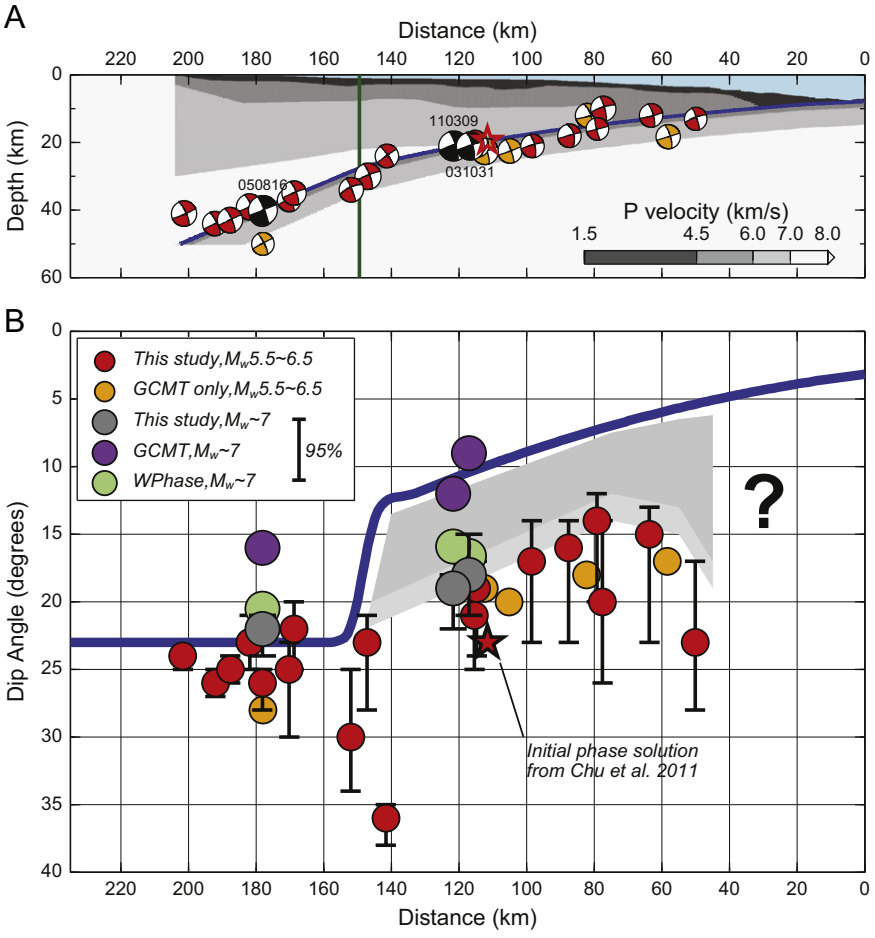

Fig. 7. (A) Colored beachballs (see the legend in Fig. 1A) show earthquakes with re-estimated depths and GCMT horizontal locations projected to the AA' profile. Red star indicates the hypocenter of the 2011 Tohoku-Oki earthquake. Green line marks the position of the kink in the reference plate interface model (blue line). (B) The comparison between dip angles from earthquake focal mechanisms (colored dots, see legend and main text for details) and the reference plate interface model (blue line). Note the jump of dip angle from 13° to 23° at the kink. Error bars show the 95% confidence limits estimated by the bootstrapping method. The GCMT and W-Phase focal mechanisms for the three M7 earthquakes are also shown for comparison. Note the ~7° systematic differences in dip between the GCMT solution and this study. Updip of the kink, the gray zone shows the 5–10° differences between the earthquake dip angles and the reference plate interface dip angle. The red star indicates the initial phase of the 2011 Tohoku-Oki earthquake modeled as an M_w 4.9 earthquake with a dip angle of 23° (Chu et al., 2011). (For interpretation of the references to color in this figure caption, the reader is referred to the web version of this article.)

Ye et al. (in press) used Empirical Green's Functions to isolate the source spectra for earthquakes in Tohoku-Oki region, and found that these earthquakes had less high-frequency energy than intra-plate earthquakes.

If these interplate events occurred on the reference plate interface as shown by the blue line in Fig. 7A, both their locations and their fault geometry should be consistent. Since the dip angle is the best constrained focal mechanism parameter, we can compare the earthquake dip angles with plate interface dip angles. In Fig. 7B, the blue line indicates the dip angle calculated from the reference plate interface model, increasing toward the coast. Note the jump of dip angle from 13° to 23° at the kink (marked by the green line in Fig. 7A). Red and dark gray dots with error bars indicate the earthquake dip angles with 95% confidence limits, for M_w 5.5–6.5 and $M_w \sim 7$, respectively. Orange dots are the five events with only GCMT solutions. For events in the western part of the AA' profile (distance > 150 km from the trench, downdip of the kink), earthquake dip angles are relatively consistent with the dip angle of the reference plate interface. However, earthquakes within a distance of 150 km from the trench (the eastern portion of AA', updip of the kink) have systematically larger dip angles than the reference plate interface dip angle, suggesting that they occurred on steeper fault planes. The minimal dip differences are ~5–10°, considering the 95% confidence limits. The dip angles from the GCMT catalog show a similar trend (Fig. S1), except for the three $M_w \sim 7$ events (purple dots in Fig. 7B) which we discuss in more detail later. In addition, the initial phase of the Tohoku-Oki earthquake can be modeled as an M_w 4.9 shallow-angle thrust event as shown by Chu et al. (2011). By modeling its teleseismic short period (0.5–2 Hz) P waveform, Chu et al. (2011) show that this beginning event also has an anomalous dip angle of 23° (red star in Fig. 7).

The GCMT dip angles for the three $M_w \sim 7$ events (purple dots in Fig. 7B) are all smaller than our inverted dip angles (gray dots in Fig. 7B) by ~7°. Note that for the two shallower events (2003/10/31, 2011/03/09), the GCMT dip angles are actually consistent with the reference plate interface dip angle, while for the deeper event (2005/08/16) the GCMT dip angle is 7° smaller than the reference plate interface. It should be noted that the GCMT depths for the two shallower events are 15 km and 14.1 km, respectively, ~6 km shallower than the reference plate interface depth (~21 km) based on their centroid locations. Due to the moment-dip-depth tradeoff, long-period moment tensor inversion could have significant dip angle bias due to the depth bias. To explore this problem, we conducted W-Phase moment tensor inversions for the three events and tested the effect of depth (Kanamori and Rivera, 2008; Duputel et al., 2012). Fig. S2 shows clear depth-dependence of dip angle and moment for the 2011/03/09 M_w 7.3 earthquake. If the depth is set above the plate interface, at 16 km, the W-Phase dip angle is about 11.5°, consistent with the GCMT solution; if depth is set at the plate interface, 21 km, the W-Phase dip angle is about 16°, close to our inverted result. The W-Phase solutions for the three $M_w \sim 7$ events with depths fixed at the reference plate interface are shown in Fig. 7B as light green dots. For the deeper 2005/08/16 M_w 7.2 earthquake, the GCMT depth is 37 km, not significantly different from the reference plate interface depth of 40 km, but still the GCMT dip angle (16°) is smaller than our inverted result (22°) and our W-Phase result (21°). For this earthquake, we have additional information from regional and local observations. The NIED F-Net moment tensor solution using regional waveforms for this earthquake has a dip angle 23°. Using an OBS network above the source area, Hino et al. (2006) show that this earthquake's aftershock sequence formed a well-defined plane, with a dip angle of 23°.

In summary, although the interplate earthquakes in this area occurred close to the reference plate interface imaged in previous seismic surveys, there is a clear depth-dependent dip angle discrepancy. Downdip of the break-point of slope (vertical green line in Fig. 7), earthquake dip angles are consistent with the reference plate interface dip angle; on the other hand, updip of the kink, all the earthquakes, including the initial phase of the 2011 Tohoku-Oki earthquake, have 5–10° steeper dip angles than the reference plate interface. Within the 95% confidence intervals, no clear lateral variation or moment dependence is observed within our study area (within 60 km from AA') and magnitude range (M_w 5.5–7.5).

5. Discussion

We discuss three possible explanations for the observed dip angle discrepancy. Both pros and cons for each explanation will be presented.

5.1. Model I: Segmented fault along dip

The reference plate interface model derived by Miura et al. (2005) has a kink at ~150 km from the trench (green line in Fig. 7A). The dip angle jumps from 13° to 23° at the kink. Using a similar dataset, Ito et al. (2005) presented a slightly different plate interface model (green line in Fig. 8A) with an additional kink at ~80 km from the trench. The dip angles of the three segments separated by the two kinks are 4°, 13° and 23°, respectively. Most of the events with steeper dip angles are located in the middle segment and have an average dip angle of 17°. Our model I for the dip angle discrepancy uses the same locations of the two kinks as in Ito et al. (2005), but has the middle segment dipping 17° to explain the earthquake dip angles (red line in Fig. 8A). We have little constraint on the dip angle of the updip segment because very few earthquakes ruptured there except the 2011 Tohoku-Oki earthquake, so we set the dip angle to be 3°, the same as the ocean floor dip just outside the trench. Compared to the plate interface model by Ito et al. (2005), the updip kink is sharper (difference in dip increases from 9° to 14°) and the downdip kink is smoother (difference in dip decreases from 10° to 6°).

In this model, the 2011 Tohoku-Oki earthquake nucleated in the middle segment (red star in Fig. 8A), but ruptured all the way to the trench with large slip (> 40 m) in the outer wedge (e.g. Lay et al., 2011; Wei et al., 2012). Complete stress release is inferred by the occurrence of many aftershocks with normal faulting mechanisms (Hasegawa et al., 2011). To explain these unique features and the long recurrence time, Fukao et al. (2011) proposed a model in which the inner and outer wedges are separated by a strong seismic barrier. In the pre-seismic stage, the seismic barrier prevented rupture in the inner wedge from propagating into the outer wedge, and accumulated stress, which was eventually released during the Tohoku-Oki earthquake. The very low dynamic basal friction in the outer wedge caused complete stress drop and very large slip. In our Model I, the sharp kink separating the inner wedge and outer wedge could act as the proposed strong seismic barrier.

The difficulty with Model I is the significant depth difference from the previous plate interface models. For distances > 120 km from the trench, Model I is ~5 km deeper than the plate interface model by Miura et al. (2005) (red and blue lines in Fig. 8A), and ~3 km deeper than the model by Ito et al. (2005) (red and green lines in Fig. 8A), which are significant differences for a seismic profile with both reflection and refraction data. Unfortunately, earthquake depth determination using either OBS data or teleseismic depth phases usually rely on the assumption of Vp/Vs ratio (e.g. Suzuki et al., in press) and hence cannot distinguish these differences conclusively.

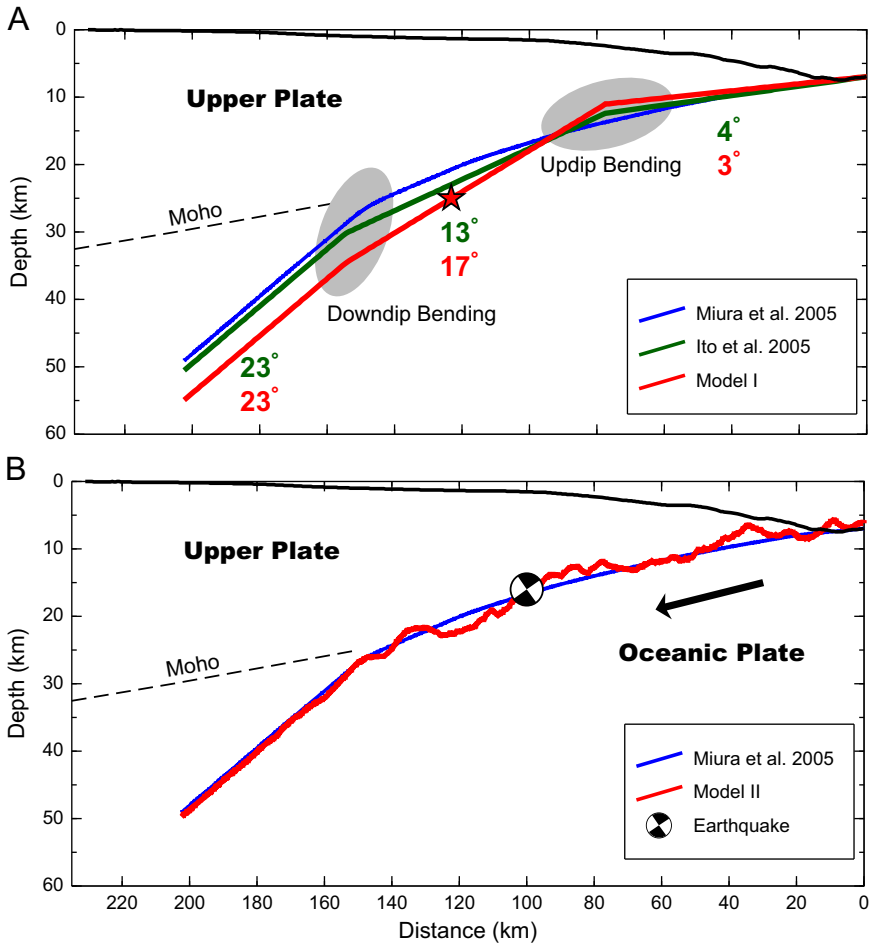

Fig. 8. Sketch of Model I and Model II. (A) Model I: Oceanic plate undergoes two points with significant changes in dip angle. The blue line shows the reference plate interface model from Miura et al. (2005). The green line indicates a slightly modified plate interface model with two kinks from Ito et al. (2005) using similar dataset. The green numbers below each segment are the dip angles, respectively. Model I is illustrated as the red line, with dip angles shown below in red numbers. The red star shows the hypocenter of the 2011 Tohoku-Oki earthquake. (B) Model II: plate interface with topography (red line). The beachball shows an earthquake occurring on the front side of a local topographic high. Note the smoother interface topography at depths greater than the Moho. (For interpretation of the references to color in this figure caption, the reader is referred to the web version of this article.)

5.2. *Model II: rough plate interface*

In Model II, we interpret these earthquakes with steeper dip angles as indicators of rough fault topography, as schematically indicated by the red line in Fig. 8B. If the plate interface has rough topography at different scales, small events may tend to occur on the front sides of local fault topography due to concentration of stress or particular orientation of the local stress tensor. These events will have steeper dip angles than the average fault dip angle. Most of the earthquakes analyzed in this study have $M_w \sim 6$, so the fault patch dimensions are on the order of 10 km, assuming a circular rupture area and "reasonable" stress drop ($\sim$3 MPa, Kanamori and Anderson, 1975). Consequently, from 5° to 10° differences in dip angle imply heights of about 1 km. Topography of this scale at depth may be hard to image in seismic reflection or refraction profiles. The consistent dip angle downdip of the kink (Fig. 7B) requires the topography to be smoother, potentially due to increased temperature, or stiffer ambient mantle material beyond the Moho discontinuity that may serve to reduce any fault roughness (Fig. 8B).

Since the earthquakes with steeper dip angles occurred in the area with large co-seismic slip in the Tohoku-Oki earthquake, Model II implies that the ruptured interface during the Tohoku-Oki earthquake was rough, and thus potentially more strongly coupled (i.e., requiring a higher stress to fail seismically) than surrounding regions. This strong coupling could explain the inferred high stress drop and by extension the long recurrence time between events. Using highly accurate relative locations, Hasegawa et al. (2007) also suggested that a geometrically irregular plate interface could explain their observations of the fault plane dip of repeating earthquakes which are believed to lie on the megathrust. Their interpretation called upon a locally coupled spot embedded in a larger creeping portion of the fault.

However, the physical origin of this local fault topography is uncertain. We note that the dimension of the smaller earthquakes is comparable to that of small seamounts (with moderate footprint, but relatively smooth topography). In other subduction margins, subducted seamounts are thought to strongly enhance plate coupling (Cloos, 1992; Scholz and Small, 1997), although some studies suggest the opposite (Mochizuki et al., 2008; Wang and Bilek, 2011). This mechanism has been previously called upon to explain the rupture regions of large earthquakes in the Costa Rica subduction zone (Bilek et al., 2003) and behavior of the rupture pattern of the 1946 M 8.1 Nankaido earthquake (Kodaira et al., 2000). Several seamounts are known to have subducted (Mochizuki et al., 2008) or are presently in the process of being subducted in the regions proximal to the 2011 Tohoku-Oki earthquake (Fig. 9A). The horst and graben structures formed in the top of the descending plate in response to extension induced as the plate bends into the subduction zone may be another

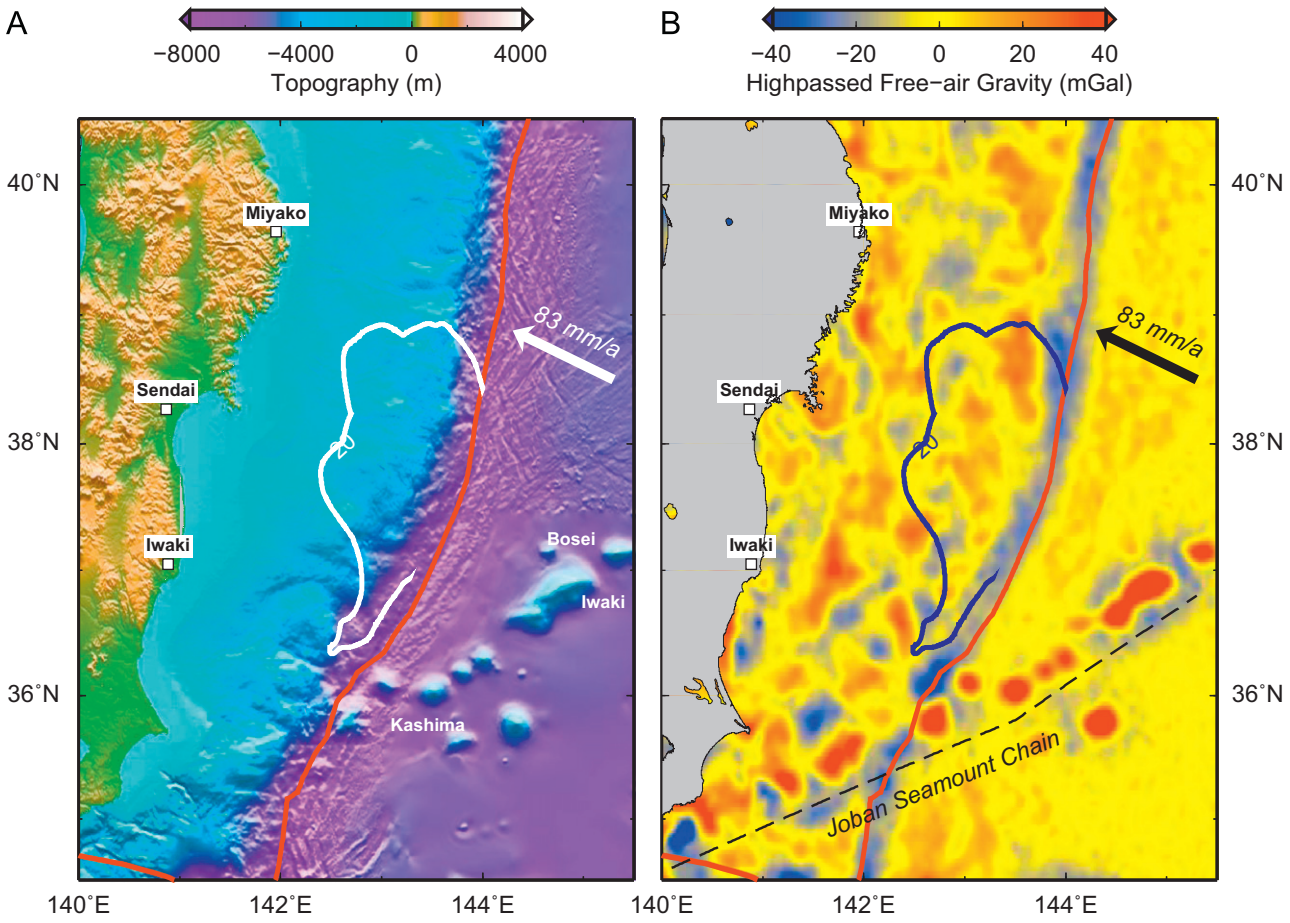

Fig. 9. A) Topography and bathymetry map of northeast Japan with identified seamounts. Red lines indicate the subduction plate boundaries and white arrow indicates the direction of convergence between the Pacific Plate and northeast Japan. The white line indicates the 20 m contour of co-seismic slip of the 2011 Tohoku-Oki earthquake (Wei et al., 2012). (B) Free air gravity field offshore Tohoku. The gravity field has been high-passed filtered with a Gaussian filter (wavelength < 50 km). Dashed line indicates the strong positive anomalies of the Joban Seamount Chain and its extension under the forearc to just offshore the Boso Peninsula. The blue line indicates the 20 m contour of co-seismic slip of the 2011 Tohoku-Oki earthquake. The black arrow indicates the direction of convergence between the Pacific Plate and northeast Japan. (For interpretation of the references to color in this figure caption, the reader is referred to the web version of this article.)

candidate for the inferred fault roughness. Such structures are clearly evident to the east of the trench in high-resolution bathymetry of the area (Fig. 1A) and have been imaged at the shallow subduction interface by previous seismic surveys (e.g. Von Huene and Culotta, 1989; Tsuru et al., 2000). The possibility of induced topography after subduction cannot be ruled out either.

One difficulty of Model II comes from the two $M_w \sim 7$ events with steeper dip angles (Fig. 7B). Clearly, $M_w \sim 7$ events have larger rupture areas than their smaller brethren. For example, Shao et al. (2011a) show that the large-slip patch of the 2011/03/09 M_w 7.3 foreshock is about 30 km along dip. Consequently, from 5° to 10° difference in dip angle implies a height of about 3 km with respect to the background. Previous seismic profiles did not run right above the two events so it is unclear whether topography of this scale exists. However, the inferred topography of 3 km is comparable to the un-subducted seamounts offshore from Iwaki, such as the Kashima Tablemount and Iwaki Seamount (Fig. 9A). These seamounts and others stand in a line that extends northeastward from the Japan Trench along the Joban Seamount Chain, which is clearly visible in a high-passed version (wavelengths less than ~50 km) of the free-air gravity field (Fig. 9B). We also observed strong bathymetric disturbance and positive gravity anomalies in the southwestward extension of the Joban Seamount Chain under the forearc to just offshore. However, in the source area of the 2011 Tohoku-Oki earthquake (marked by the 20 m co-seismic slip contour in Fig. 9), we do not observe a significant bathymetric disturbance or gravity anomaly of similar amplitude. If subducted seamounts are the reason for the inferred rough fault surface, they must be sufficiently small in amplitude or of neutral enough density as to not have an obvious signature in the bathymetry or gravity field.

Model II makes several other predictions, which cannot be tested with the available observations. First, a rough plate interface may produce more diverse dip angles for smaller earthquakes ($M_w < 5.5$), rather than always steeper. Second, the dip angle difference for $M_w > 5.5$ should be moment-dependent. As the rupture area increases, the average dip angle should converge to the background dip angle as imaged in seismic surveys. Within the 95% confidence interval, we are currently unable to observe such dependence.

5.3. Model III: subfaults

In Model III, the earthquakes with steeper dip angles do not occur on the plate interface as imaged by Miura et al. (2005), but instead occur on steeper nearby subfaults (Fig. 10A). While such subfaults have not been imaged, if there is no strong velocity contrast across these subfaults, previous seismic surveys might not be able to image them. Since the $M_w \sim 6$ earthquake depths may only be systematically shallower than the plate interface by ~1 km in Model III, current earthquake location accuracy is

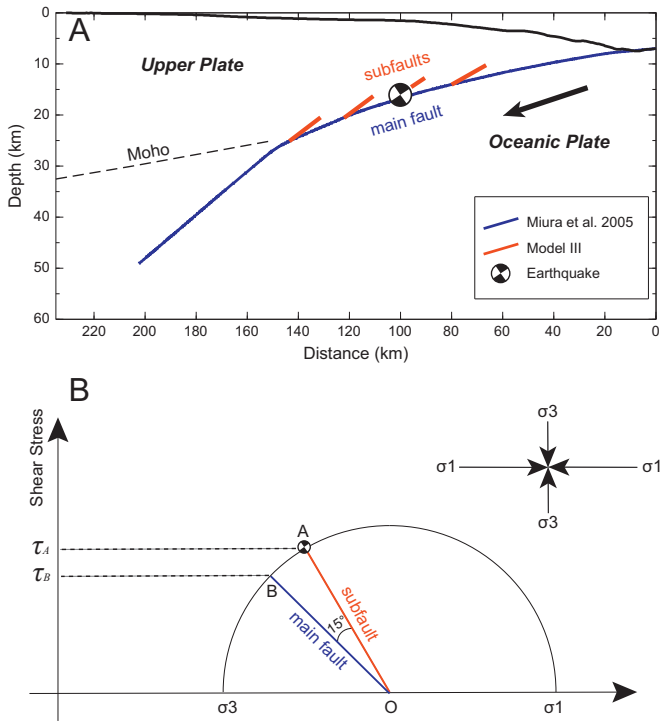

Fig. 10. Model III: Subfaults. (A) Earthquakes with steeper dip angles (black beachball) occurred on steeper subfaults (red lines) near the main fault (blue line). Note the absence of subfaults beyond the Moho or the kink. (B) Mohr diagram showing a simple mechanical model consistent with earthquakes on the steeper dipping subfaults (red lines and black beachball at point A), rather than on the main fault (blue, point B). (For interpretation of the references to color in this figure caption, the reader is referred to the web version of this article.)

insufficient to determine if they are off the main fault. For the two $M_w \sim 7$ earthquakes, the centroid depth differences could be more significant, but their depths are even harder to estimate due to their longer durations.

These steeper subfaults might reflect deep basal duplexes, formed by thrust sheets bounded from below by the plate interface and from above by a shallower décollement. Deep extensive underplating through duplexes has been observed in present and ancient accretionary prisms, as in the Costa Rica forearc, the Kodiak Islands in Alaska and the Kii Peninsula in southwest Japan (e.g. Hashimoto and Kimura, 1999; Sample and Fisher, 1986; Silver et al., 1985), and has been successfully reproduced by sandbox experiments (Gutscher et al., 1998; Kukowski et al., 2002).

Although the suggested geometry resembles splay fault-main fault junction, these subfaults may not be related to splay faults in the forearc wedge. In the same region as this study, Tsuji et al. (2011) find splay faults only within ~60 km of the trench (outer wedge), while most of the events studied in this paper are >60 km away from the trench (inner wedge). The outer wedge and inner wedge are separated by a steeply dipping normal fault. Seismic reflection profiles in other regions, such as the Nankai subduction zone (Park et al., 2002) and Sunda margin (Kopp and Kukowski, 2003), show similar widths of outer wedges containing extensive splay faulting. Wang and Hu (2006) proposed that the inner wedge generally stays in the stable regime, while the outer wedge undergoes active deformation.

Considering the uncertainty of our dataset, here we only explore a simple mechanical model with a uniform stress field. The maximum and minimum principal stresses σ_1 and σ_3 are assumed to be sub-horizontal and sub-vertical, respectively, perpendicular to the trench (Fig. 10B). Since all of the earthquakes with steeper dip angles occurred before the 2011 Tohoku-Oki earthquake, this assumption is reasonable (e.g. Hasegawa et al., 2011). Red line OA in Fig. 10B indicates the stress state of the subfaults. Since the main fault's dip angle is on average 7.5° (5–10°) smaller than the subfaults, we need to rotate OA in Fig. 10B by 15° to OB to obtain the shear stress on the main fault. With the assumed stress orientation, the shear stress on the subfault (τ_A in Fig. 10B) is always larger than the shear stress on the main fault (τ_B). Thus, earthquakes can occur on the subfaults rather than on the nearby main fault even if the strength of the main fault is slightly smaller than that of the subfaults. However, since the average difference in the dip angles is only 7.5°, the difference in shear stress ($\tau_A - \tau_B$) is also small. This suggests that the main fault's strength is actually comparable to that of the nearby subfaults.

One possible interpretation of this behavior is as follows. Since observations of the 2011 Tohoku-Oki earthquake suggest high stress drop, the main fault may have healed to a relatively strong fault during the interseismic period preceding the 2011 Tohoku-Oki earthquake. The megathrust fault zone may not be a well-defined interface, but may be a zone with a finite thickness in which both the "main fault" and the "subfaults" exist (e.g. basal duplexes). As commonly suggested for weak megathrust faults (e.g. Magee and Zoback, 1993; Wang and Suyehiro, 1999) and weak strike-slip faults (e.g. Hardebeck and Hauksson, 1999), relatively uniform pore-pressure and/or frictional properties within this fault zone may cause them to have about the same strength. To contain the anomalous M7 earthquakes, the fault zone would need to be ~3 km thick, at least locally. This kind of fault zone structure may have been imaged in some subduction zones, such as the 3–5 km thick ultra-slow velocity layer in southern Mexico (Song et al., 2009), and the low velocity zone imaged in Cascadia (Calvert et al., 2011). One possible scenario is that most earthquakes before the 2011 Tohoku-Oki earthquake preferentially occurred on the subfaults as discussed above until finally the main fault failed either by triggering from the subfault earthquakes or by local weakening on the main fault.

6. Conclusions

In this paper, we determine the locations and focal mechanisms of M_w 5.5–7.5 earthquakes in the source region of the 2011 Tohoku-Oki earthquake using teleseismic waveforms. Although the interplate earthquakes in this area occurred close to the plate interface imaged in previous seismic surveys, there is a clear depth-dependent dip angle discrepancy. All the earthquakes in the region that experienced large-slip during the M_w 9.1 event, including the initial phase of the 2011 Tohoku-Oki earthquake, have 5–10° steeper dip angles than the reference plate interface dip angle. This discrepancy cannot be explained by a single smooth plate interface. We provide three possible explanations.

In Model I, the oceanic plate undergoes two distinct changes in dip. These two geometric discontinuities may have acted as strong seismic barriers in previous seismic ruptures, but may have failed in and contributed to the Tohoku-Oki earthquake's rupture.

In Model II, the discrepancy of dip angles is due to a rough plate interface, which in turn may be the underlying cause for the overall strong coupling and concentrated energy-release.

In Model III, the earthquakes with steeper dip angles did not occur on the plate interface imaged before, but on nearby steeper subfaults. Since the differences in dip angle are on average only 7.5°, this explanation implies that the main fault has almost the same strength as the nearby subfaults, rather than much weaker. A relatively uniform thick fault zone with both the "main fault" and the "subfaults" inside is consistent with this model.

To distinguish between these different models, detailed study of seismic structure, gravity and magnetic anomalies, especially in the source areas of the anomalous M7 earthquakes, is necessary. Since the physical reason for this dip angle discrepancy is still unclear, approaches relying solely on earthquake focal mechanisms to constrain plate interface geometry may be problematic, as previously pointed out by Hayes et al. (2009).

Acknowledgment

We thank Seiichi Miura, Narumi Takahashi, Aki Ito and Ryota Hino for providing their velocity models or earthquake catalog. We thank Robert Graves, another anonymous USGS internal reviewer and two anonymous reviewers for their comments that improved the manuscript. The Incorporated Research Institutions for Seismology (IRIS) provided the seismic data. All figures are made with GMT. This work is supported by the National Science Foundation through grant number EAR-1142020. Contribution #10080 of the Tectonic Observatory, California Institute of Technology.

Appendix A. Supporting information

Supplementary data associated with this article can be found in the online version at http://dx.doi.org/10.1016/j.epsl.2012.07.038.

References

Ammon, C.J., Lay, T., Kanamori, H., Cleveland, M., 2011. A rupture model of the 2011 off the Pacific coast of Tohoku Earthquake. Earth Planets Space 63, 693–696.
Bilek, S.L., Schwartz, S.Y., DeShon, H.R., 2003. Control of seafloor roughness on earthquake rupture behavior. Geology 31, 455.
Brocher, T.M., 2005. Empirical relations between elastic wavespeeds and density in the Earth's crust. Bull. Seismol. Soc. Am. 95, 2081–2092.
Calvert, A.J., Preston, L.A., Farahbod, A.M., 2011. Sedimentary underplating at the Cascadia mantle-wedge corner revealed by seismic imaging. Nat. Geosci. 4, 545–548.
Chu, R., Wei, S., Helmberger, D.V., Zhan, Z., Zhu, L., Kanamori, H., 2011. Initiation of the great M_w 9.0 Tohoku-Oki earthquake. Earth Planet. Sci. Lett., 308.
Cloos, M., 1992. Thrust-type subduction-zone earthquakes and seamount asperities: a physical model for seismic rupture. Geology 20, 601.
DeMets, C., Gordon, R.G., Argus, D.F., 2010. Geologically current plate motions. Geophys. J. Int. 181, 1–80.
Duputel, Z., Rivera, L., Kanamori, H., Hayes, G., 2012. W-phase fast source inversion for moderate to large earhquakes (1990–2010). Geophys. J. Int. 189 (2), 1125–1147.
Fukao, Y., Hori, T., Kodaira, S., 2011. The 2011 M_w9.0 Tohoku-Oki Earthquake: Joint Occurrence of Tectonic Stress-Driven and Lithostatic Stress-Driven Slips Along the Plate Boundary, AGU 2011 Fall Meeting, San Francisco, California.
Gutscher, M.-A., Kukowski, N., Malavieille, J., Lallemand, S., 1998. Episodic imbricate thrusting and underthrusting: Analog experiments and mechanical analysis applied to the Alaskan Accretionary Wedge. J. Geophys. Res. 103, 10161–10176.
Hardebeck, J.L., Hauksson, E., 1999. Role of fluids in faulting inferred from stress field signatures. Science 285, 236–239.
Hasegawa, A., Uchida, N., Igarashi, T., Matsuzawa, T., Okada, T., Miura, S., Suwa, Y., 2007. Asperities and quasi-static slips on the subducting plate boundary east off Tohoku, NE Japan. SEIZE volume. Columbia University Press.
Hasegawa, A., Yoshida, K., Okada, T., 2011. Nearly complete stress drop in the 2011 A/w 9.0 off the Pacific coast of Tohoku Earthquake. Earth Planets Space 63, 703.
Hashimoto, Y., Kimura, G., 1999. Underplating process from melange formation to duplexing: Example from the Cretaceous Shimanto Belt, Kii Peninsula, southwest Japan. Tectonics 18, 92–107.
Hayes, G.P., Wald, D.J., Keranen, K., 2009. Advancing techniques to constrain the geometry of the seismic rupture plane on subduction interfaces a priori: higher-order functional fits. Geochem. Geophys. Geosyst. 10, Q09006.
Helmberger, D.V., Engen, G.R., 1974. Upper mantle shear structure. J. Geophys. Res. 79, 4017–4028.
Hino, R., Yamamoto, Y., Kuwano, A., Nishino, M., Kanazawa, T., Yamada, T., Nakahigashi, K., Mochizuki, K., Shinohara, M., Minato, K., 2006. Hypocenter distribution of the main-and aftershocks of the 2005 Off Miyagi Prefecture earthquake located by ocean bottom seismographic data. Earth Planets Space 58, 1543.
Ide, S., Baltay, A., Beroza, G.C., 2011. Shallow dynamic overshoot and energetic deep rupture in the 2011 M_w 9.0 Tohoku-Oki Earthquake. Science 332, 1426–1429.
Ito, A., Fujie, G., Miura, S., Kodaira, S., Kaneda, Y., Hino, R., 2005. Bending of the subducting oceanic plate and its implication for rupture propagation of large interplate earthquakes off Miyagi, Japan, in the Japan Trench subduction zone. Geophys. Res. Lett. 32, L05310.
Kagan, Y.Y., 2003. Accuracy of modern global earthquake catalogs. Phys. Earth Planet 135, 173–209.
Kanamori, H., Anderson, D.L., 1975. Theoretical basis of some empirical relations in seismology. Bull. Seismol. Soc. Am. 65, 1073.
Kanamori, H., Given, J.W., 1981. Use of long-period surface waves for rapid determination of earthquake-source parameters. Phys. Earth Planet 27, 8–31.
Kanamori, H., Rivera, L., 2008. Source inversion of W phase: speeding up seismic tsunami warning. Geophys. J. Int. 175, 222–238.
Kikuchi, M., Kanamori, H., 1982. Inversion of complex body waves. Bull. Seismol. Soc. Am 72, 491–506.
Komatitsch, D., Tromp, J., 1999. Introduction to the spectral element method for three-dimensional seismic wave propagation. Geophys. J. Int. 139, 806–822.
Kodaira, S., Takahashi, N., Nakanishi, A., Miura, S., Kaneda, Y., 2000. Subducted seamount imaged in the rupture zone of the 1946 Nankaido earthquake. Science 289, 104.
Koper, K.D., Hutko, A.R., Lay, T., Ammon, C.J., Kanamori, H., 2011. Frequency-dependent rupture process of the 2011 M_w 9.0 Tohoku Earthquake: Comparison of short-period P wave backprojection images and broadband seismic rupture models. Earth Planets Space 63, 599–602.
Kopp, H., Kukowski, N., 2003. Backstop geometry and accretionary mechanics of the Sunda margin. Tectonics 22, 1072.
Kukowski, N., Lallemand, S.E., Malavieille, J., Gutscher, M.A., Reston, T.J., 2002. Mechanical decoupling and basal duplex formation observed in sandbox experiments with application to the Western Mediterranean Ridge accretionary complex. Mar. Geol 186, 29–42.
Lay, T., Ammon, C.J., Kanamori, H., Xue, L., Kim, M.J., 2011. Possible large near-trench slip during the 2011 M_w 9.0 off the Pacific coast of Tohoku Earthquake. Earth Planets Space 63, 687–692.
Lay, T., Kanamori, H., Ammon, C.J., Koper, K.D., Hutko, A.R., Ye, L., Yue, H., Rushing, T.M., 2012. Depth-varying rupture properties of subduction zone megathrust faults. J. Geophys. Res. 117, B04311.
Magee, M.E., Zoback, M.D., 1993. Evidence for a weak interplate thrust fault along the northern Japan Subduction zone and implications for the mechanics of thrust faulting and fluid expulsion. Geology 21, 809–812.
Minoura, K., Imamura, F., Sugawara, D., Kono, Y., Iwashita, T., 2001. The 869 Jogan tsunami deposit and recurrence interval of large-scale tsunami on the Pacific coast of northeast Japan. J. Natural Disaster Sci. 23, 83.
Miura, S., Takahashi, N., Nakanishi, A., Tsuru, T., Kodaira, S., Kaneda, Y., 2005. Structural characteristics off Miyagi forearc region, the Japan Trench seismogenic zone, deduced from a wide-angle reflection and refraction study. Tectonophysics 407, 165–188.
Mochizuki, K., Yamada, T., Shinohara, M., Yamanaka, Y., Kanazawa, T., 2008. Weak interplate coupling by seamounts and repeating $M\sim$ 7 earthquakes. Science 321, 1194.
Ozawa, S., Nishimura, T., Suito, H., Kobayashi, T., Tobita, M., Imakiire, T., 2011. Coseismic and postseismic slip of the 2011 magnitude-9 Tohoku-Oki earthquake. Nature 475, 373–376.
Park, J.O., Tsuru, T., Kodaira, S., Cummins, P.R., Kaneda, Y., 2002. Splay fault branching along the Nankai subduction zone. Science 297, 1157.
Sample, J., Fisher, D., 1986. Duplex accretion and underplating in an ancient accretionary complex, Kodiak Islands, Alaska. Geology 14, 160–163.
Sato, M., Ishikawa, T., Ujihara, N., Yoshida, S., Fujita, M., Mochizuki, M., Asada, A., 2011. Displacement above the hypocenter of the 2011 Tohoku-Oki earthquake. Science 332, 1395.
Scholz, C.H., Small, C., 1997. The effect of seamount subduction on seismic coupling. Geology 25, 487.
Shao, G., Ji, C., Zhao, D., 2011a. Rupture process of the 9 March, 2011 M_w 7.4 Sanriku-Oki, Japan earthquake constrained by jointly inverting teleseismic waveforms, strong motion data and GPS observations. Geophys. Res. Lett. 38, L00G20.
Shao, G., Li, X., Ji, C., Maeda, T., 2011b. Focal mechanism and slip history of the 2011 M_w 9.1 off the Pacific coast of Tohoku Earthquake, constrained with teleseismic body and surface waves. Earth Planets Space 63, 559.
Silver, E.A., Ellis, M.J., Breen, N.A., Shipley, T.H., 1985. Comments on the growth of accretionary wedges. Geology 13, 6–9.
Simons, M., Minson, S.E., Sladen, A., Ortega, F., Jiang, J., Owen, S.E., Meng, L., Ampuero, J.-P., Wei, S., Chu, R., Helmberger, D.V., Kanamori, H., Hetland, E., Moore, A.W., Webb, F.H., 2011. The 2011 Magnitude 9.0 Tohoku-Oki Earthquake: Mosaicking the Megathrust from seconds to centuries. Science 332, 1421–1425.
Song, T.-R.A., Helmberger, D.V., Brudzinski, M.R., Clayton, R.W., Davis, P., Perez-Campos, X., Singh, S.K., 2009. Subducting slab ultra-slow velocity layer coincident with silent earthquakes in southern Mexico. Science 324, 502–505.
Suzuki, K., Hino, R., Ito, Y., Suzuki, S., Inazu, D., Iinuma, T., Fujimoto, H., Shinohara, M., Kaneda, Y.. Seismicity near hypocenter of the 2011 off the Pacific coast of Tohoku earthquake deduced by using Ocean Bottom Seismographic data. Earth Planets Space, http://dx.doi.org/10.5047/eps.2012.04.010, in press.

Takahashi, N., Kodaira, S., Nakanishi, A., Park, J.-O., Miura, S., Tsuru, T., Kaneda, Y., Suyehiro, K., Kinoshita, H., Hirata, N., Iwasaki, T., 2002. Seismic structure of western end of the Nankai trough seismogenic zone. J. Geophys. Res. 107, 2212.

Tichelaar, B.W., Ruff, L.J., 1989. How good are our best models? Jackknifing, bootstrapping, and earthquake depth. Eos. Trans. AGU 70 (20), 593–606.

Tsai, V.C., Hayes, G.P., Duputel, Z., 2011. Constraints on the long-period moment-dip tradeoff for the Tohoku earthquake. Geophys. Res. Lett. 38, L00G17.

Tsuji, T., Ito, Y., Kido, M., Osada, Y., Fujimoto, H., Ashi, J., Kinoshita, M., Matsuoka, T., 2011. Potential tsunamigenic faults of the 2011 off the Pacific coast of Tohoku Earthquake. Earth Planets Space 63, 831–834.

Tsuru, T., Park, J.-O., Takahashi, N., Kodaira, S., Kido, Y., Kaneda, Y., Kono, Y., 2000. Tectonic features of the Japan Trench convergent margin off Sanriku, northeastern Japan, revealed by multichannel seismic reflection data. J. Geophys. Res. 105 (B7), 16,403–16,413.

Usami, T., 1966. Descriptive table of major earthquakes in and near Japan which were accompanied by damages. Bull. Earthquake Res. Inst. 44, 1571–1622.

Von Huene, R., Culotta, R., 1989. Tectonic erosion at the front of the Japan Trench convergent margin. In: Cadet, J.P., Uyeda, S. (Eds.), Subduction Zones: the Kaiko Project. Tectonophysics, 160; 1989, pp. 75–90.

Wang, K., Bilek, S.L., 2011. Do subducting seamounts generate or stop large earthquakes? Geology 39, 819.

Wang, K., Hu, Y., 2006. Accretionary prisms in subduction earthquake cycles: the theory of dynamic Coulomb wedge. J. Geophys. Res. 111, B06410.

Wang, K., Suyehiro, K., 1999. How does plate coupling affect crustal stresses in Northeast and Southwest Japan. Geophys. Res. Lett. 26, 2307–2310.

Wei, S., Graves, R., Helmberger, D.V., Avouac, J.-P., Jiang, J., 2012. Sources of shaking and flooding during the Tohoku-Oki earthquake: a mixture of rupture styles. Earth Planet. Sci. Lett., 333–334, 91–100.

Wu, W., Ni, S., Zhan, Z., A three-dimensional hybrid method for modeling teleseismic body waves with complicated source-side structure, in preparation.

Ye, L., Lay, T., Kanamori, H.. Ground shaking and seismic source spectra for large earthquakes around the megathrust fault offshore of Northeastern Honshu, Jpn. Bull. Seismol. Soc. Am., in press.

Zhao, D., Huang, Z., Umino, N., Hasegawa, A., Kanamori, H., 2011. Structural heterogeneity in the megathrust zone and mechanism of the 2011 Tohoku-oki earthquake (M_w 9.0). Geophys. Res. Lett. 38, L17308.